



Stent Porosity Efficiency in Treating Wide-Neck Saccular Renal Artery Aneurysm

H. Abu Bakar¹, A. Abas^{1†} and N. Razak²

¹*School of Mechanical Engineering, Universiti Sains Malaysia, Engineering Campus, 14300 Nibong Tebal, Pulau Pinang, Malaysia*

²*School of Aerospace Engineering, Universiti Sains Malaysia, Engineering Campus, 14300 Nibong Tebal, Pulau Pinang, Malaysia*

†*Corresponding Author Email: aizatabas@usm.my*

(Received May 21, 2019; accepted September 29, 2019)

ABSTRACT

Renal arteries are the arteries that supply blood to the kidneys. Renal artery aneurysm (RAA) is the second most common visceral aneurysm to occur, which accounts for 22% of the visceral aneurysm. In general population, RAA rate of occurrence was only 0.1%. However, due to the extensive use of angiography technique, RAA has been discovered more frequently. Some claimed that the previous rate of incidence should be higher now because of the capability of angiography. The rupture of this aneurysm could result in haemorrhage, kidney lost and mortality. The size of the renal artery which is different compared to other types of arteries such as the abdominal aorta could produce different flow condition when the artery is inflicted with RAA condition. Thus, a thorough analysis is desired as RAA studies are very limited compared to other aneurysm conditions. In this study, the efficiency of the stent porosity was investigated in treating the RAA. Fluid-structure interaction (FSI) simulations and particle image velocimetry (PIV) experiments were the approaches taken to investigate the flow patterns of the blood when the stent of different porosities was placed in the aneurysm entrance. The effect of wall shear stress (WSS), the deformation of the artery and von Mises stress were also observed in determining the possibility of aneurysm rupture. The study found that the placement of stent of different porosities succeeds in providing an obstruction to the blood from circulating inside the aneurysm sac. This in turns reduced the WSS experienced by the aneurysm sac up a significant value of 96%. This reduction is crucial in order to prevent the aneurysm from rupture. Moreover, the placement of the stent provided support to the renal artery and preventing it from experiencing buckling failure. The maximum deformation of the artery reduced by 42% with stent was placed in the renal artery. In fact, the von Mises stress decreased below the threshold limit of 0.5 MPa with the presence of the stent. In addition, the study found that the stent of porosity 80% has a similar impact to the stent of lower porosity in the case of RAA at main renal artery.

Keywords: Renal artery aneurysm; Porosity; FSI; PIV.

NOMENCLATURE

p pressure
v velocity

Δt time interval
 Δx fluid displacement
 ρ density

1. INTRODUCTION

The arteries that supply blood to the kidneys are known as the renal arteries. Renal arteries bifurcate from the abdominal artery and link to the kidneys. Renal artery aneurysm (RAA) is a balloon-like bulging at a particular point along the artery vessel due to the weakening of the vessel muscle (Hafizah Mokhtar *et al.* 2017). The most common RAA is of saccular shape, which is a berry-shaped bulge at one side of the artery (Eskandari *et al.* 2005). RAA

commonly occurs in pregnant women and if the aneurysm ruptures due to increase in blood pressure, it could be fatal for the patients and the baby (Maughan *et al.* 2015). In addition, total loss of the kidney could also occur due to the occurrence (Maughan *et al.* 2015). According to Klausner *et al.* (2015), RAA incidence only happens around 0.1% of the general population of the world. This may be the reason why the study of RAA is rather limited as compared to other aneurysm conditions.

Currently, there are no FSI study focusing on a wide-

neck, saccular renal artery aneurysm (RAA) at the main renal artery. Most of the studies regarding renal artery aneurysm (RAA) are in the likes of retrospective studies (Barros *et al.* 2014; Coleman *et al.* 2015; Gates *et al.* 2017; Wang *et al.* 2018) or case studies (Canyigit M *et al.* 2015; Chandra *et al.* 2014; Hwang *et al.* 2011; Maughan *et al.* 2015; Sousa *et al.* 2017; Sultan *et al.* 2016). The FSI study is important to understand the mechanism of rupture of aneurysm at renal artery especially in the case of wide-neck aneurysm (Canchi *et al.* 2015). Relying solely on the diameter of the aneurysm for rupture risk assessment is not sufficient as it been claimed by many researches in other aneurysm conditions (Canchi *et al.* 2015; Farotto *et al.*, 2018; Rissland *et al.*, 2009; Sharzehee *et al.* 2018; Stergiou *et al.* 2019).

It is noteworthy to mention that the different size of renal artery as compared to other artery such as abdominal aorta, could produce different flow condition, which in turn would yield different outcomes if the aneurysm is present in that artery. For instance, the abdominal aortic aneurysm size requires proper intervention at a size of 8.0 cm in diameter having a rupture rate of 50% (Aggarwal *et al.* 2011). On the contrary, the intervention for RAA is needed when the aneurysm size reached more than 2 cm or patients with hypertension symptom (Soliman *et al.* 2006). Thus, a separate study is required in order to analyse the RAA condition. There are two methods in treating aneurysms. The conventional one is the open surgery treatment (Orion *et al.* 2013). At present, the most preferable approach is the EVAR method (Hafizah Mokhtar *et al.* 2017). EVAR or Endovascular treatment is a feasible technique, where a mesh-like tube called stent is inserted into the aneurysm-damaged artery with the hope to provide a proper pathway of the blood flowing through the artery and blocking it from circulating inside the aneurysm. Canton *et al.* (2005) believed that simply blocking the aneurysm with one or more stents may disturb the blood flow into the aneurysm sac, which in turn will reduce the intra-aneurysmal flow velocity inside it thereby resulting to formation of thrombus. At present, there are also no FSI study on the treatment of renal artery aneurysm (RAA) using stent as well as most of the studies regarding RAA are more focusing on the generality of the disease and case study as mentioned previously. This study is also crucial to ensure the capability of stent to treat a wide-neck, saccular aneurysm cases especially at main renal artery.

In this research, the effectiveness of stents with different porosity is studied with the aim of blocking the blood circulating inside aneurysm and to promote thrombus formation. It is noteworthy to mention that numerical simulation had been frequently used by many researchers of aneurysm. According to Hoi Yiemeng *et al.* (2004), computational method such as CFD and FSI can be used to accurately model complex behaviour of the blood flow, in which the parameters of fluid dynamics and the blood particle paths can be calculated and visualised. Hoi Yiemeng *et al.* (2004) studied the effects of local vessel curvature and aneurysm neck size on the hemodynamic of an aneurysm using CFD analysis.

Drewe *et al.* (2017) studied the effects of proximal neck and iliac bifurcation angle of the AAA using FSI approach. The wall stress and the hemodynamic of the blood were analysed based on the varied parameters. Yeow *et al.* (2016) applied CFD method to study the effects of stent graft placement on the hemodynamic of the blood for AAA. Lin *et al.* (2017a) implemented few modelling techniques to determine the best model to represent the real event. The methods used in their study are FSI, computational fluid dynamic (CFD) and computational solid stress (CSS). Based on their findings, FSI simulations showed a closer and more accurate results as compared to the other two methods.

2. METHODOLOGY

2.1 Fluid-Structure Interaction

Fluid-structure interaction is the coupling of finite volume and finite element methods in order to study the effects of fluid to the structure and vice versa. The fluid pressure and forces will be subjected to the solid as it flows through it leading to the deformation of the solid. This fluid-structure interaction causes the flow of the fluid to be disturbed as well. This phenomenon needs to be captured for a reliable and accurate results to be produce. In this study, a two-way FSI simulation is performed. Figure 1 shows the general overview of the two-way FSI process.

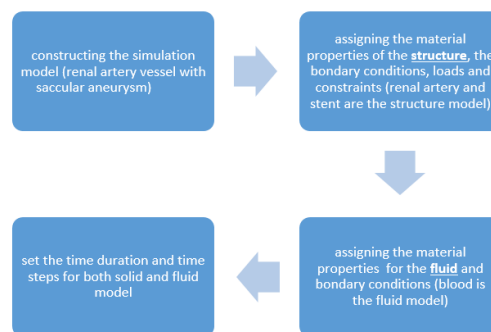


Fig. 1. General overview of the two-ways FSI setup process.

2.1.1 Fluid Formulations

For the fluid side, two fundamental governing equations used are the Navier-Stokes and continuity equations. The equations are as follow:

Navier-Stokes equation

$$\rho \left(\frac{dv}{dt} + v \cdot \nabla v \right) = \nabla p + \mu \nabla^2 v \quad (1)$$

Continuity equation

$$\frac{\delta \rho}{\delta t} + \nabla \cdot (\rho v) \quad (2)$$

with ρ representing the blood's density, v is the blood's velocity, whereas p is the blood's pressure.

In ANSYS Fluent, Semi-Implicit Method (SIMPLE) solver was used to solve the governing equation by

solving the pressure-velocity coupling. It is a predictor-corrector approach where it used the relationship between velocity and pressure correction to enforce the mass conservation and obtaining the pressure field. The approximation of the velocity field is obtained through solving the momentum equation while the pressure gradient is obtained through the pressure distribution from either the initial guess or from the previous iteration. After that, the pressure equation is formulated and solved and a new pressure distribution is obtained. The velocity will be corrected and a new set of conservative fluxes is calculated.

In this study, for simplicity, blood will be considered as Newtonian fluid with density of 1050 kg/m³ and dynamic viscosity of 0.0035 Pa.s (Javadzadegan *et al.* 2014; Ou *et al.* 2017; Suess *et al.*, 2016). Moreover, Suess *et al.* (2016) claimed that the effect of non-Newtonian characteristic is influential only when the diameter of the vessel is less than 1 mm.

2.1.2 Structural Formulation

For the structural side, the displacement of the structural body is governed using the following equation:

Displacement equation

$$\rho^s \frac{D^2 u}{Dt^2} - \nabla \cdot (F \cdot S(u)) = \rho^s b^s \tag{3}$$

With *u* denoting the displacement of the structural body, *b^s* is the body forces applied to the structure, *S* is the second Piola-Kirchhoff stress tensor, *ρ^s* is the structure’s density and *F* represents gradient tensor deformation.

2.1.3 Fluid-Structure Interaction Analysis

In ANSYS, a partitioned approach is used to solve the fluid-structure interaction analysis. The method solved the fluid and structural equations separately using separate solver. This means that it solved the two systems of equations separately but with shared boundary conditions. The advantage of this approach is it increased the capabilities of evolution and optimization of each code.

2.2 Model Construction

The RAA used was based on idealised model and the dimensions were taken from one of the case study by Bracale *et al.* (2017). The patient data was taken from a wide-necked right RAA with a diameter of 28×24 mm. Table 1 shows the dimension of the RAA model drawn using SolidWorks 2017. The fluid domain was constructed in ANSYS Fluent. Figure 2 shows the 3-D models for structural and fluid parts. The stent is designed using SolidWorks 2017 in which the distance between each diamond-shaped hole is varied in order to produce different porosity. The porosity percentages are varied from 65% to 80% and calculated through the following equation:

$$\text{porosity percentage} \% = \frac{\text{area of stent not covered by metal}}{\text{total area of stent}} \tag{4}$$

The material used for the FD is cobalt chromium. It is one of the common material used in the

development of FD (Alderazi *et al.* 2014; Brouillard *et al.* 2016; Rajah *et al.* 2017; Suzuki *et al.* 2017). The material properties are taken from Suzuki *et al.* (2017) and are tabulated in Table 2.

Table 1 Dimension of renal artery aneurysm

Renal artery aneurysm diameter	28 × 24 mm
Thickness of renal artery	0.5 mm
Length of renal artery	65 mm
Density	1000 kg/m ³

Table 2 Material properties of cobalt chromium Suzuki *et al.* (2017)

Density	10,000 kg/m ³
Poisson ratio	0.26
Yield tensile strength	470 MPa
Ultimate tensile strength	1130 MPa
Young modulus	206,000 MPa

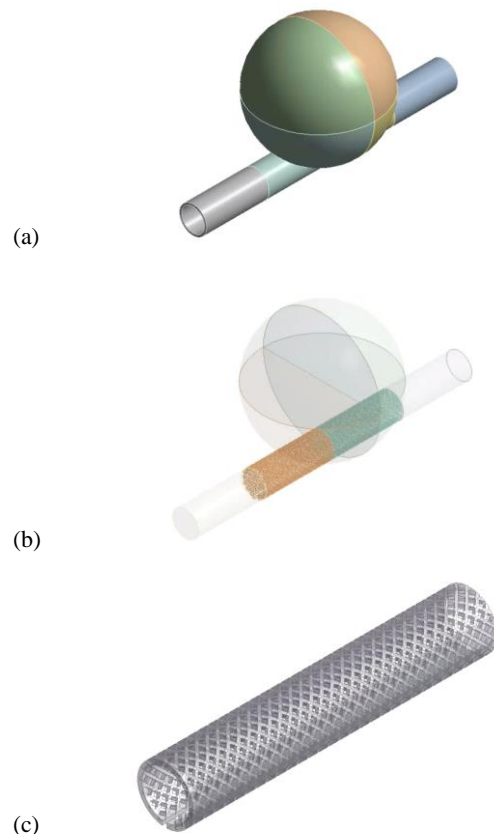


Fig. 2. (a) 3-D model of the RAA; (b) 3-D model of the blood domain; (c) stent design.

Hyper-elastic model was chosen as the material properties for renal artery, as done by Valencia *et al.* (2013). In their previous work, Valencia *et al.* (2013)

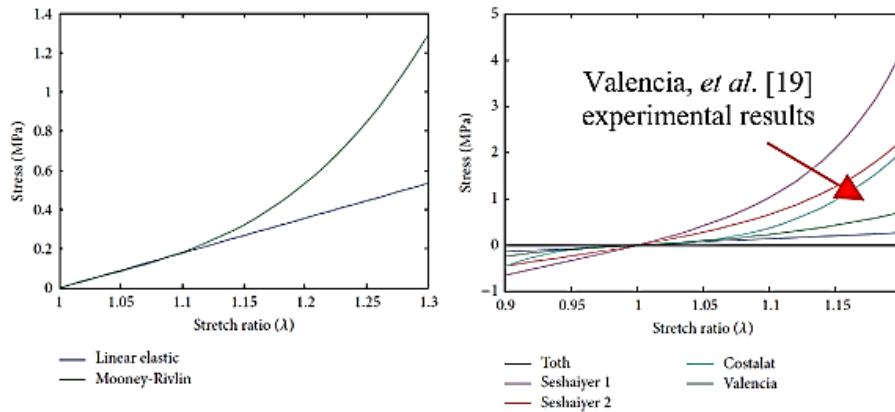


Fig. 3. Comparison of stress vs. stretch ratio of Mooney-Rivlin hyper-elastic model (left) and Valencia, *et al.* (2013) experimental result.

conducted an experiment in determining the mechanical behaviour of the aneurysm wall through traction testing machine. The experimental result showed a similar pattern with Mooney-Rivlin hyper-elastic material properties data of stress versus stretch ratio, as depicted in Fig. 3. The strain energy function ω is given in the model by:

$$\omega(\lambda) = C_{10}(I_1 - 3) + C_{01}(I_2 - 3) + C_{11}(I_1 - 3)(I_2 - 3) + C_{20}(I_1 - 3)^2 + C_{02}(I_2 - 3)^2 \quad (5)$$

where I_1 and I_2 are the 1st and 2nd strain invariants of the Cauchy-Green deformation tensor C_{ij} . C_{10} , C_{01} , C_{11} , C_{20} , C_{02} are the material constants stated in Table 2.

$$C_{ij} = 2\varepsilon_{ij} + \delta_{ij} \quad (6)$$

where δ_{ij} is the Kronecker delta.

Table 3 Fitting coefficients of hyperelastic Mooney-Rivlin five-parameters model

Coefficient	MPa
C_{10}	0.3848
C_{01}	-0.0891
C_{11}	0.5118
C_{20}	0.5109
C_{02}	0.4912

2.3 Boundary Conditions

2.3.1 Structural Model

The boundary conditions were setup in ANSYS Transient Structural. Both ends of the artery were assigned as fixed support. This means that the surfaces has zero degree of freedom. The surfaces inside that were in contact with the fluid domain were assigned as ‘Fluid-structure interface’ condition. Figure 4(a) depicted the assigned boundary conditions for structural model.

2.3.2 Fluid Domain

For the fluid domain, ANSYS Fluent setup was used

to incorporate the boundary conditions. The inlet and outlet were assigned to be in pulsatile condition. For the inlet, a pulsatile velocity inlet with maximum velocity of 0.5 m/s and minimum velocity of 0.1 m/s were set. The outlet boundary condition was assigned as pulsatile outlet pressure with maximum pressure of 12 kPa and minimum pressure of 9 kPa. The pulsatile flow formulation was based on Sinnott *et al.* (2006) with a heart rate of 60 bpm, representing a normal heart rate of an adult. The ‘fluid-structure interface’ surfaces are selected as well during fluent setup so that the data transfer between structural and fluid solver can happen. Figure 4(b) shows the assigned boundary condition for fluid model.

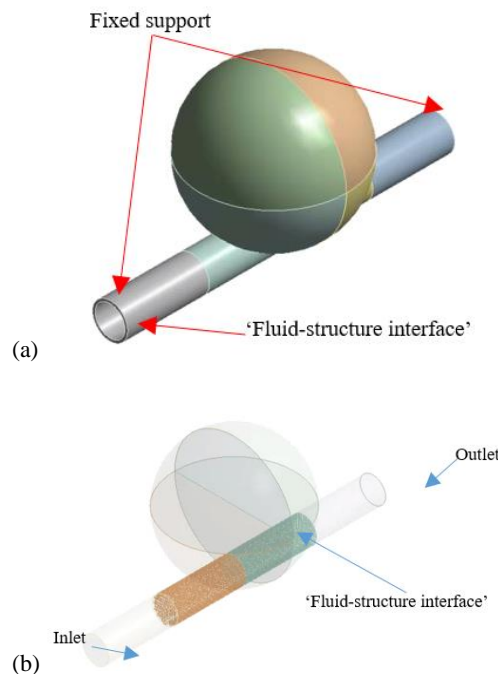


Fig. 4. Boundary conditions for: (a) structural model; (b) Blood domain.

Semi-Implicit Method (SIMPLE) algorithm scheme is used to solve the pressure-velocity coupling.

SIMPLE is based on the predictor-corrector approach. It uses a relationship between velocity and pressure corrections to enforce mass conservation and to obtain the pressure field. The approximation of the velocity field is obtained by solving the momentum equation and the pressure gradient term is obtained by using the pressure distribution from either the initial guess of the previous iteration. Then, the pressure equation is formulated and solved and a new pressure distribution is obtained. The velocities are then corrected and a new set of conservative fluxes is calculated.

2.5 Mesh Convergence Analysis

Mesh convergence analysis is a process of optimization of the mesh used for the simulation process. To optimize between computation time and accuracy of the results, the size of the mesh was varied and the changes in velocity were tracked to see at which point it converges. A smaller mesh will improve the accuracy of the results but it will cost a higher computational time. Hence, it is crucial to find the optimization point where the results is accurate enough with low computational time.

The meshing of the fluid domain was done in the ANSYS Fluent mesh setup. Mesh sizes starting from $1 \cdot 10^{-2}$ m to $3 \cdot 10^{-4}$ m were tested and compared in Table 4. Based on Fig. 5, it shows that the velocity results saturates at mesh size of $7 \cdot 10^{-4}$ m with a minimal error of 2.57%. Thus, for further simulations in this research, the mesh size of $7 \cdot 10^{-4}$ m will be used to minimize the computation time.

Table 4 Mesh convergence analysis data

Fluid domain			
Mesh size (m)	Num. of elements	Maximum velocity (m/s)	Percentage difference (%)
$1 \cdot 10^{-2}$	11,207	0.4521	-
$1 \cdot 10^{-3}$	24,391	0.5817	14.93
$7 \cdot 10^{-4}$	67,107	0.6041	2.57
$5 \cdot 10^{-4}$	156,930	0.6052	0.85
$3 \cdot 10^{-4}$	215,348	0.6063	0.74

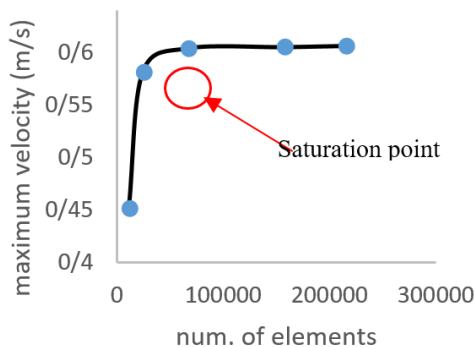


Fig. 5. Convergence graph of number of element against maximum velocity.

2.6 Particle Image Velocimetry Experiment (PIV)

Particle image velocimetry (PIV) is an optical method of tracking and studying flow pattern. The particles are mixed with the working fluid used. As it flows through the region of interest, light pulses from laser will illuminate the particles while a camera captured the movement of those particles. From the consecutive images between two light pulses, the particles' movement can be traced through:

$$V = \frac{\Delta x}{\Delta t} \quad 7$$

where Δx is the particles displacement and Δt is the interval time. The working fluid in this experiment was aqueous glycerol solution, which is a mixture of 22% of glycerol by mass with water. This is to mimic blood characteristic, where the density and viscosity of the solution becomes 1059 kg/m^3 and $1.562 \cdot 10^{-6} \text{ m}^2/\text{s}$ respectively.

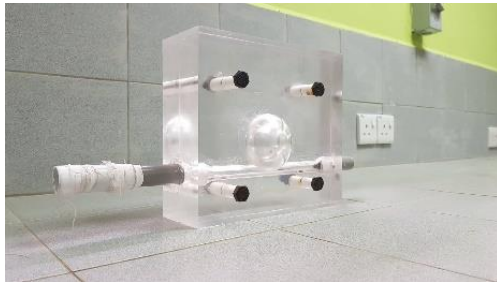
The seeding particle used is PSP-50 (Polymide seeding particles from Dantec Dynamics) with a diameter of $50 \mu\text{m}$. The laser model is NANO L135-15 PIV with pulse duration of 4 ns. The camera used is Dantec HiSense MKII C8484-05CP with a frame rate of 12.2 fps at full resolution. The interval time between images was set at 163 ms with 20 frames, which means 10 images captured for each image acquisition process. Figure 6 depicted the RAA model, PIV setup and flow process of the PIV experiment. For the RAA model, CNC machining is used to cut the two Perspex block of dimension $223 \times 200 \times 40 \text{ mm}$. The Perspex blocks were joined together using bolts and nuts. In addition, silicone sealants are applied to prevent leakage of the fluid. Figure 6 (a) is the RAA model. The method of using Perspex as a model for PIV experiment has been done by many researchers (Hafizah Mokhtar *et al.* 2017; Mokhtar *et al.* 2016; Raschi *et al.* 2012; Tateshima *et al.* 2002).

The size of the model has been scaled-up by a factor of 2.5. The geometry of the real scale has to be increased with ratio 2.5:1. Next, the dimensionless number, Reynolds number has to be preserve to produce similar flow behaviour in real and scaled-up cases. This resulted in the flow rate of the flow in the experiment to be 2 l/min to maintain the Reynolds number of 900.

The PIV experiment started by pumping the aqueous glycerol solution to the RAA model. A valve and flow meter are connected to Arduino Uno R3 board to produce the pulsatile flow as well as to monitor the instantaneous flow rate of the solution. Then, the laser light is activated to illuminate the seeding particles while the camera captures the flow pattern. The flow patterns and velocity magnitude were compared between the simulations and PIV experimental results. The simulations will be considered reliable and accurate if it managed to produce comparable results as obtained in PIV experiment.

The parameter chosen for comparison between the simulation and experiment data is the maximum

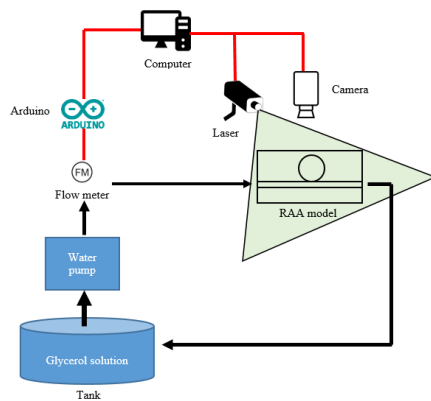
velocity of the blood flow. The reason behind taking maximum velocity as our comparison parameter is because the maximum velocity of the blood can either promote fast thrombosis and increase the rate of occlusion of the aneurysm or it can increase the potential rupture due to the increased in WSS and stress of the wall applied by the flow of blood. This aligned with the findings by (Kulcsar *et al.* 2012; Mut *et al.* 2015).



(a)



(b)



(c)

Fig 6. (a) RAA model for the PIV experiment; (b) PIV setup; (c) Flow process of the PIV experiment.

3. RESULTS AND DISCUSSIONS

The purpose of this study is to analyze the effectiveness of stent with different porosities for the treatment of RAA condition. The flow patterns and velocities of the fluid, wall shear stress (WSS), deformation of the RAA and von Mises stress are the variables that will be examined.

3.1 PIV Validation

PIV experiment was conducted to validate the simulation results and to prove its reliability and accuracy. The comparison between the PIV and simulation results are done at only one time point, which is at the peak systole where the flow reached the maximum velocity. Table 5 depicts the comparison between simulation and experimental results on the velocity parameter. There are small similarities in the velocity contours for both simulation and experiment (circle in red in Table 5). But the overall comparison showed that there exist flow circulation inside the aneurysm dome. The maximum velocity obtained in the simulation is 0.0276 m/s while in the PIV experiment is 0.0264 m/s. The percentage difference of maximum velocity between the simulations and PIV experiment is 4.36%. Therefore, it is believed that the simulations results is in good agreement with the experiment data in term of the maximum velocity.

3.2 Flow Pattern

In this section, comparisons of flow patterns and maximum velocities were conducted for all stents of different porosities. Figure 7 shows the locations where the velocity values were taken in order to observe the velocity flow inside the aneurysm sac and Table 6 is the results tabulated. Table 7 shows the velocity contours for all cases from time 1.0 s to 2.0 s. For the case of RAA model without any stent placement, it was observed that the blood tends to flow and circulate inside the aneurysm dome. In contrast, when a stent is placed at the entrance of the aneurysm, the blood flow is blocked from entering the aneurysm and the stents are capable of obstructing the blood from circulating inside the aneurysm that is located in a straight main renal artery with no tortuous or complex geometry. The flow velocity inside the aneurysm or intra-sac velocity reduced greatly when a stent was placed inside the RAA model. Even for the largest porosity percentage stent, it managed to prevent the blood from entering the aneurysm sac. The velocity contour distribution for all stent cases are comparable throughout the period of 1.0 s to 2.0 s. In Table 6, it is shown that the percentage difference of velocity inside the aneurysm sac reduced greatly with most of it reached the percentage difference of 80%.

This findings proved that stent placement succeed in its purpose to block blood from entering and circulating inside the aneurysm. This results agreed with the statement by Ngoepe *et al.* (2018), which stated that the purpose of stent placement is to alter the hemodynamic of the blood by reducing the flow in the aneurysm dome and redirecting it along the main artery vessel. Ngoepe *et al.* (2018) also stated that a reduced flow inside the aneurysm sac will result in clot formation, which is the desirable condition for recovery of aneurysm. Sisto *et al.* (2015) stated the same point, in which the reduced intra-sac velocity will promote thrombus formation inside the aneurysm. Kulcsar *et al.* (2012) and Aird (2007) also stated that slow blood flow is an important factor for promoting thrombosis.

Table 5. Comparison of velocity contours for simulation and PIV experiment

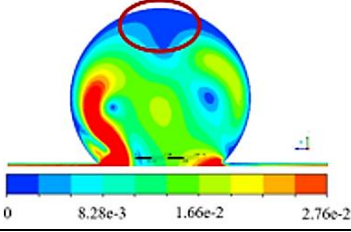
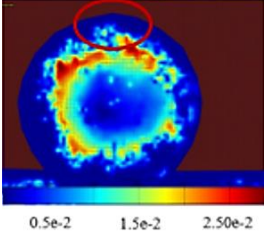
Case (Scale-up factor of 2.5)	Max. velocity (m/s)	Velocity contours	Percentage difference (%)
Simulation	0.0276		-
PIV experiment	0.0263		4.36

Table 6. Velocities comparison at locations inside the aneurysm sac. The percentage difference is the comparison of velocity between each case with the case of RAA without any stent placement

Velocity at location (m/s)	Cases			
	65%	70%	75%	80%
1	0.0585	0.0012	0.0074	0.0037
Percentage difference (%)	-	97.98%	87.43%	93.73%
2	0.0467	0.0074	0.0066	0.0109
Percentage difference (%)	-	84.23%	85.91%	76.69%
3	0.0164	0.0017	0.0027	0.0026
Percentage difference (%)	-	89.55%	83.83%	84.41%
4	0.0138	0.0003	0.0004	0.0002
Percentage difference (%)	-	97.85%	96.78%	98.29%
5	0.0557	0.0027	0.0055	0.0037
Percentage difference (%)	-	95.11%	90.06%	93.42%
6	0.0595	0.0050	0.0027	0.0075
Percentage difference (%)	-	91.65%	95.54%	87.41%

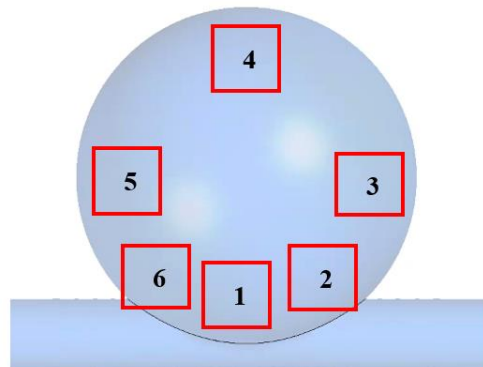
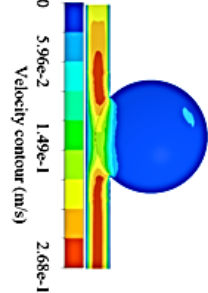
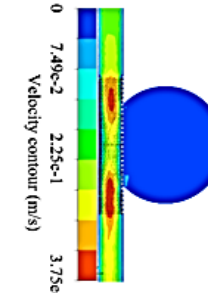
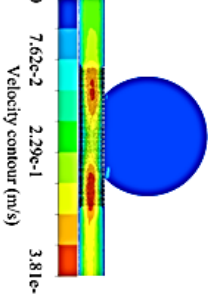
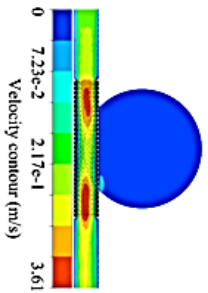
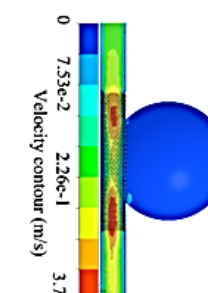
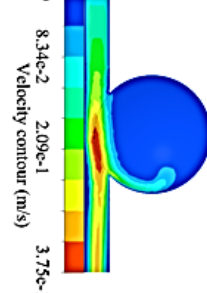
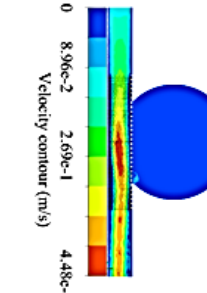
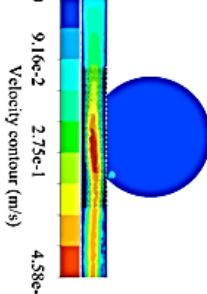
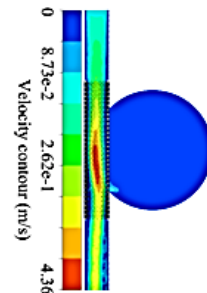
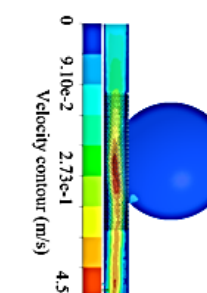
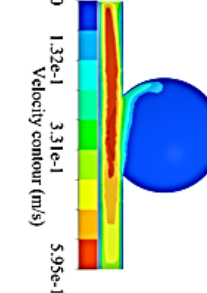
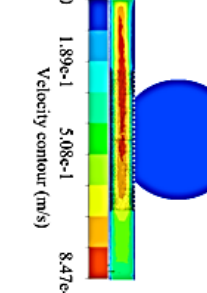
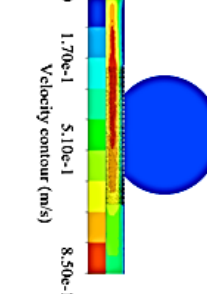
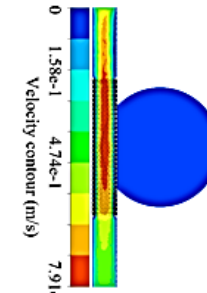
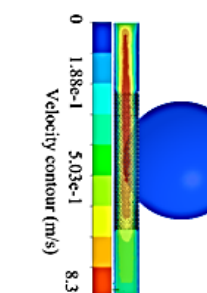


Fig. 7. Locations where the velocity values extracted in the aneurysm sac.

Table 7 Velocity contour for all cases from time 1.0 s to 2.0 s

Time (s)	RAA	FD 65%	FD70%	FD 75%	FD 80%
1.0	 <p>Velocity contour (m/s) 0 5.96e-2 1.49e-1 2.68e-1</p>	 <p>Velocity contour (m/s) 0 7.49e-2 2.23e-1 3.75e-1</p>	 <p>Velocity contour (m/s) 0 7.62e-2 2.29e-1 3.81e-1</p>	 <p>Velocity contour (m/s) 0 7.23e-2 2.17e-1 3.61e-1</p>	 <p>Velocity contour (m/s) 0 7.53e-2 2.26e-1 3.76e-1</p>
1.2	 <p>Velocity contour (m/s) 0 8.34e-2 2.09e-1 3.75e-1</p>	 <p>Velocity contour (m/s) 0 8.96e-2 2.69e-1 4.48e-1</p>	 <p>Velocity contour (m/s) 0 9.16e-2 2.75e-1 4.58e-1</p>	 <p>Velocity contour (m/s) 0 8.73e-2 2.62e-1 4.36e-1</p>	 <p>Velocity contour (m/s) 0 9.10e-2 2.73e-1 4.55e-1</p>
1.4	 <p>Velocity contour (m/s) 0 1.32e-1 3.31e-1 5.95e-1</p>	 <p>Velocity contour (m/s) 0 1.89e-1 5.08e-1 8.47e-1</p>	 <p>Velocity contour (m/s) 0 1.70e-1 5.10e-1 8.50e-1</p>	 <p>Velocity contour (m/s) 0 1.58e-1 4.74e-1 7.91e-1</p>	 <p>Velocity contour (m/s) 0 1.88e-1 5.03e-1 8.39e-1</p>

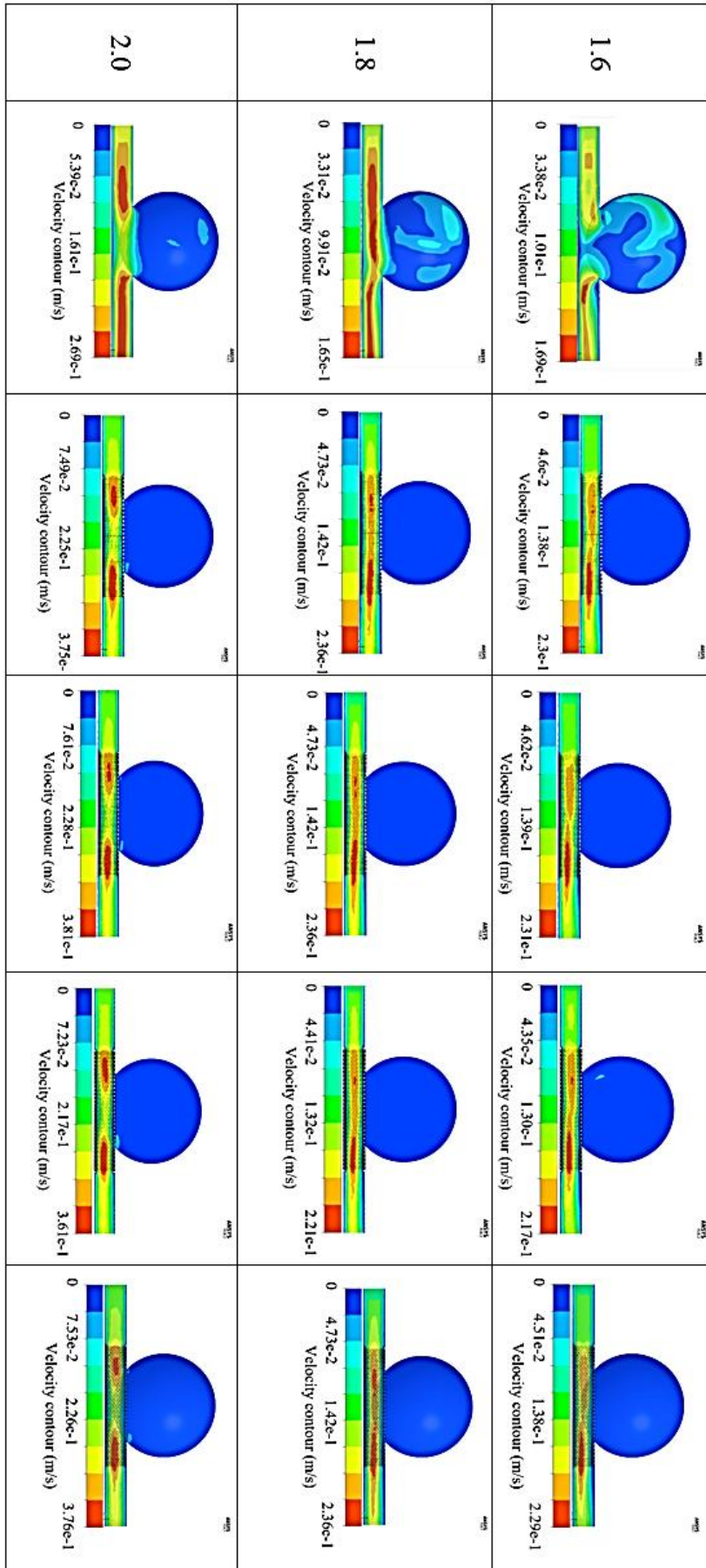


Table 8 Maximum WSS at stent and aneurysm sac for all cases

Case	Maximum WSS at Stent (Pa)	Maximum WSS at aneurysm sac (Pa)
RAA only	-	5.777
RAA + stent porosity 65%	5.0	0.2
RAA + stent porosity 70%	5.0	0.2
RAA + stent porosity 75%	6.0	0.2
RAA + stent porosity 80%	6.5	0.2

Table 9 Wall shear stress (WSS) contours for all cases

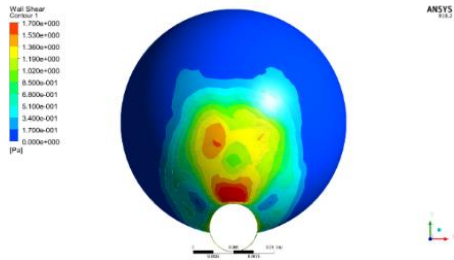
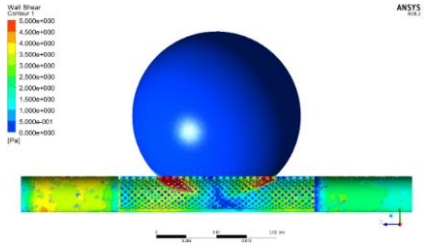
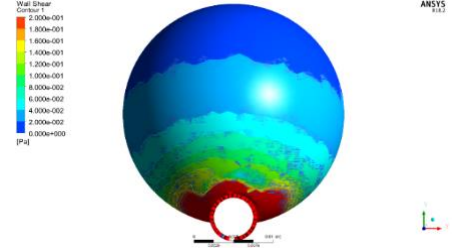
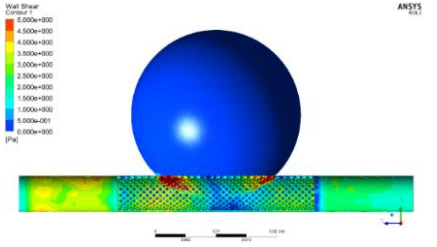
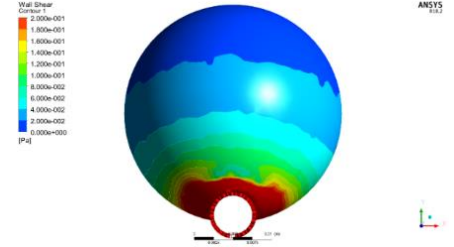
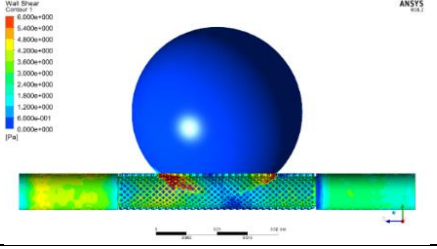
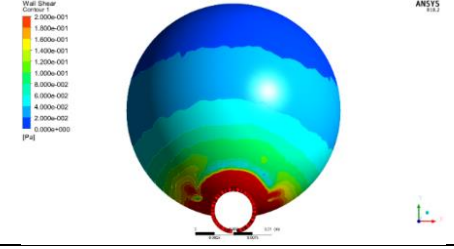
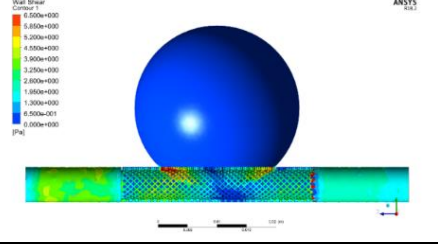
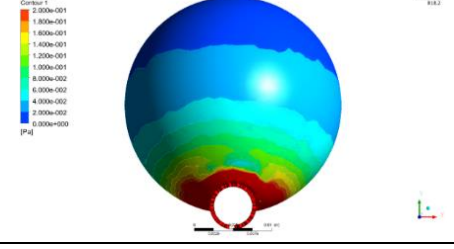
Case	Maximum shear stress at FD	Maximum shear stress at aneurysm
RAA	N/A	
FD 65%		
FD 70%		
FD 75%		
FD 80%		

Table 10 Deformations for all cases and the percentage difference of stent cases against case of RAA without stent

case	total deformation (mm)	Percentage difference (%)
RAA	1.3270	-
Stent 65%	0.7982	39.85%
Stent 70%	0.7980	39.86%
Stent 75%	0.8000	39.72%
Stent 80%	0.7699	41.98%

Table 11 Deformation contours for all simulated cases

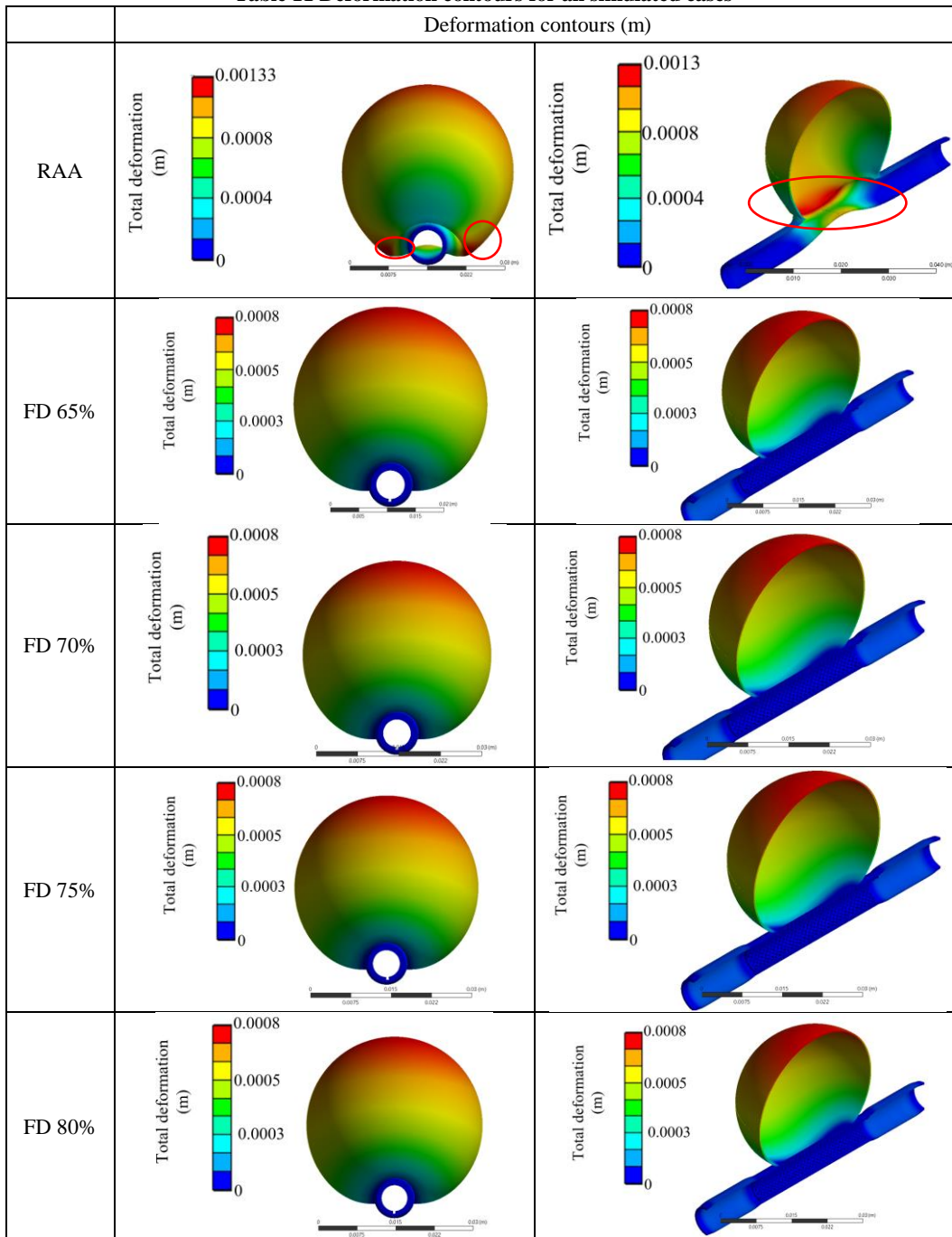


Table 12 Von Mises contours for all simulated cases

case	Maximum von Mises stress (Pa)	
	FD model	RAA model
RAA	N/A	
FD 65%		
FD 70%		
FD 75%		
FD 80%		

Table 13 Maximum von Mises stress for all cases

Cases	FD model	Percentage difference (%) (vs. FD cases)	RAA model
RAA	-	-	1.738E6
65%	12.364	-	31.292
70%	13.370	8.14	30.606
75%	14.327	7.16	26.094
80%	23.128	61.43	27.88

3.3 Wall Shear Stress (WSS) of the Aneurysm

In this section, two locations of WSS are observed, which is at the aneurysm sac and at the stent. Table 8 is the maximum WSS recorded at the stent and the aneurysm sac. While Table 9 shows the WSS contours for all cases simulated.

Based on Table 8 and 9, the aneurysm sac experienced greater WSS for the case where there is no stent placement in the RAA model. However, when a stent is placed, a significant reduction of maximum WSS was recorded, as tabulated in Table 8. A percentage difference of approximately 96% was obtained. This significant reduction of WSS due to the blockage of blood from entering the aneurysm dome by the stent. The WSS contours distribution for all stent cases seems comparable where there is minimum WSS at the aneurysm sac and maximum WSS occurred at the stent, at the region where the entrance of the aneurysm sac is located. The findings show that the greater the porosity percentage, the greater the WSS at stent.

The reduction of WSS is crucial as it can be a factor of aneurysm ruptures. According to [Du *et al.* \(2017\)](#), WSS of 1.5 Pa is adequate to degenerate the endothelial cells at the aneurysm wall, which in turn will cause the formation of lesion and rupture. [Hoi Yiemeng *et al.* \(2004\)](#) stated that the baseline level for WSS is between 15 – 20 dynes/cm² (1.5 – 2.0 Pa). In this study, the WSS recorded for the case of RAA without stent reached up to 5.0 Pa. This value is far beyond the threshold limit set by [Du *et al.* \(2017\)](#); [Hoi Yiemeng *et al.* \(2004\)](#). The large WSS could trigger the matrix metalloproteinase production through the smooth muscle cells, which in the end will damage the elastic lamina and cell apoptosis ([Varble *et al.*, \(2017\)](#)).

3.4 Deformation of the Renal Artery Aneurysm

Table 10 are the tabulated data of maximum deformations occurred for the RAA model as the blood flows through. Without the stent in the RAA model, the deformation is the greatest, with a value of 0.001327 m (1.327 mm). The aneurysm expanded up to 1.327 mm because of the blood circulation inside the aneurysm sac. In addition, a buckling effect was seen for the RAA without stent case as well (Table 11, red circles). However, when a stent

is placed in the RAA model, the buckling effect was avoided and a percentage difference of approximately 40% was achieved in all stents. Stent of porosity percentage 80% recorded the highest percentage difference in deformation of the model, which is 41.98%, from 1.327 mm to 0.76986 mm. Based on Table 11, the maximum deformation occurred at the top of the aneurysm sac. The presence of stent provided positive impact by reducing the deformation occurred at the aneurysm effected artery.

Our findings agreed with [Lin *et al.* \(2017b\)](#), for the case of without stent placement in which the aneurysm was subjected to a continuous forces to the aneurysm wall causing it to increase in diameter. Similarly [Sharzehee *et al.* \(2018\)](#) also recorded the same discoveries, where the aneurysmal artery experienced a buckling behaviour in their detailed study relating to the steady-state and pulsatile flow of the blood in the blood vessel with aneurysm present.

3.5 Von Mises Stress

Table 12 describes von Mises stress distribution contours for the RAA model and stent. Table 13 shows the maximum von Mises stress for all cases. The RAA model experienced the largest stress when there is no placed stent in the artery. The region where the maximum stress occurred was at the neck of the aneurysm. This is in agreement with the findings by [Otsuka *et al.* \(2011\)](#); [Steiger *et al.* \(1989\)](#). When a stent is placed, the RAA model was subjected to a minimal stress. However, a greater stress was seen experienced by the stent as the blood flows through it. Stent of porosity percentage of 80% recorded the highest von Mises stress magnitude with a value of 23.128 MPa. The von Mises stress contours distribution at stent are comparable for all cases.

According to [Azar *et al.* \(2018\)](#), one of the predicting factor of the aneurysm rupture is the ultimate strength tissue of the aneurysm wall. Stress subjected to the aneurysm sac that exceed its ultimate strength threshold limit will results in aneurysm rupture. In their study ([Azar *et al.* 2018](#)), the threshold limit was 1 MPa and it exceeded could causes rupture to the aneurysm. [Giannoglou *et al.* \(2006\)](#) stated in their study that the stress value could not exceed 0.65 MPa. [Di Martino *et al.* \(2006\)](#) and [Steiger *et al.* \(1989\)](#) set the threshold limit of 0.54 MPa and 0.5

MPa respectively. Based on these threshold limit, the lowest threshold limit was chosen (0.5 MPa) to avoid underestimation of the stress effect to the aneurysm sac. Thus, if the stent is not placed, the aneurysm has a greater potential to rupture due to the stress experienced was two times greater than the threshold limit value (23.128 MPa vs. 0.5 MPa). The presence of stent as seen in the data tabulated in Table 12 and 13 show that the maximum von Mises stress experienced by the aneurysm reduced desirably and that the stent served its purpose of treating the aneurysm.

For the stress experienced by the FD, the stress subjected is still below the ultimate strength of the stent material (Cobalt chromium) which indicated that the FD will be capable in withstanding the stresses when it is implanted in the renal artery.

The limitation of the current study is the simplified version of the renal artery aneurysm (RAA) that did not incorporate curvature shape to be simulated using FSI technique. In this study, the focus will be on wide-neck, saccular aneurysm located at a straight renal artery vessel. The curved geometry of the renal artery such as the ones generated from CT data would produce different flow patterns, hence different results in terms of the stent performance. This research however is concerted on the aneurysm that occurs at the main renal artery. As a basis and initial study for renal artery aneurysm (RAA) which should provide a good platform of a more complex geometry study of renal artery aneurysm e.g. curved geometry in the near future. Moreover, the use of curved shape geometry is unsuitable for the current stent porosity due to the increase in porosity area. According to Meng *et al.* (2006), the stent capability to redirect flow reduces with increasing curvature of the vessel and the stent potential efficacy to promote thrombosis diminished for aneurysm located at this curve region.

4. CONCLUSION

This study aimed at investigating the capability of stent of different porosities in treating renal artery aneurysm (RAA) condition. A fluid-structure interaction simulations were performed on an idealised model of RAA for the cases of with and without the stent placement inside the artery. Four different stent porosities were tested ranging from 65% to 80% and parameters such as flow patterns, wall shear stress (WSS), deformation of the RAA and von Mises stress were analysed.

Our study found that the stent placement at the entrance of the aneurysm sac managed to provide an obstruction to the blood from circulating inside the aneurysm dome. In addition to it, the intra-aneurysmal sac velocity was greatly reduced by the stent that is present in the RAA model. It was also observed that there is minimal difference of the results produced by stent of porosity 65% (lowest porosity percentage) and 80% (highest porosity percentage) in terms of the flow patterns and the capability of stent in blocking the blood from flowing inside the aneurysm. For the WSS, it was

seen that a significant reduction of WSS at the aneurysm sac was recorded with nearly 96% in reduction. This indicates the success of stent in preventing the blood from entering the aneurysm dome. This reduction is important to prevent the aneurysm from rupturing which could be fatal.

In terms of the deformation experienced by the RAA model simulated, the study found that the stent provided a support to the main artery thereby preventing it from buckling failure. In addition, the maximum deformation subjected to the RAA model is greatly reduced with percentage difference up to 42%. The von Mises stress also managed to be reduced from exceeding the threshold limit of 0.5 MPa when the stent was placed in the RAA model. Moreover, the study concluded that the stent of porosity 80% has similar impact to the stent of lower porosity percentage (65%).

This findings are hope to be of contribution to the clinical practice especially in the designing stent to treat renal artery aneurysm (RAA). Stent of porosity 80% is sufficient to treat aneurysm located at main renal artery without the need to use a lower porosity stent (65%).

REFERENCES

- Aggarwal, S., A. Qamar, V. Sharma, and A. Sharma, (2011). Abdominal aortic aneurysm: A comprehensive review. *Experimental and clinical cardiology* 16(1), 11-15.
- Aird, W. C. (2007). Vascular bed-specific thrombosis. *Journal of Thrombosis and Haemostasis* 5 Suppl 1, 283-291.
- Alderazi, Y., D. Shastri, T. Kass-Hout, C. Prestigiacomo, and C. D. Gandhi, (2014). Flow Diverters for Intracranial Aneurysms. *Stroke research and treatment*.
- Azar, D., D. Ohadi, A. Rachev, J. F. Eberth, M. J. Uline, and T. Shazly, (2018). Mechanical and geometrical determinants of wall stress in abdominal aortic aneurysms: A computational study. *PLOS ONE* 13(2), e0192032.
- Barros, K. J. F., P. B. Metzger, F. H. Rossi, T. O. Rodrigues, S. M. Moreira, , A. C. G. Petisco, A. M. Kambara, (2014). Techniques and Strategies for the Endovascular Treatment of Renal Artery Aneurysm. *Revista Brasileira de Cardiologia Invasiva* (English Edition), 22(1), 64-72.
- Bracale, U. M., D. Narese, I. Ficarelli, M. De Laurentis, F. Spalla, E. Dinoto, G. Vitale, D. Solari, G. Bajardi and F. Pecoraro, (2017). Stent-assisted detachable coil embolization of wide-necked renal artery aneurysms. *Diagnostic and Interventional Radiology* 23(1), 77-80.
- Brouillard, A. M., X. Sun, A. H. Siddiqui, and N. Lin, (2016). The Use of Flow Diversion for the Treatment of Intracranial Aneurysms: Expansion of Indications. *Cureus* 8(1), e472.

- Canchi, T., S. D. Kumar, E. Y. K. Ng, and S. Narayanan, (2015). A Review of Computational Methods to Predict the Risk of Rupture of Abdominal Aortic Aneurysms. *BioMed Research International* 2015, 1-12.
- Canton, G., D. I. Levy, J. C. Lasheras, and P. K. Nelson, (2005). Flow changes caused by the sequential placement of stents across the neck of sidewall cerebral aneurysms. *Journal of Neurosurg* 103(5), 891-902.
- Canyiğit, M., Çam A., Çetin H., Altunoğlu A., and M., Hıdıroğlu (2015). The use of the Cardiatis multilayer flow modulator stent to treat sequential saccular aneurysms of the renal artery in a solitary kidney. . *turkish journal of thoracic and cardiovascular surgery* (23), 354-358.
- Chandra, V., B. W. Ullery, and J. T. Lee, (2014). Endovascular Stent-Graft Repair of Proximal Renal Artery Aneurysms. *Journal of Vascular Surgery* 60(2), 546-547.
- Coleman, D. M., and J. C. Stanley, (2015). Renal artery aneurysms. *Journal of Vascular Surgery* 62(3), 779-785.
- Di Martino, E. S., A. Bohra, J. P. Vande Geest, Gupta, M. S. Makaroun, and D. A. Vorp, (2006). Biomechanical properties of ruptured versus electively repaired abdominal aortic aneurysm wall tissue. *Journal of Vascular Surgery* 43(3), 570-576.
- Drewe, C. J., L. P. Parker, L. J. Kelsey, P. E. Norman, J. T. Powell, and B. J. Doyle, (2017). Haemodynamics and stresses in abdominal aortic aneurysms: A fluid-structure interaction study into the effect of proximal neck and iliac bifurcation angle. *Journal of Biomechanics*, 60 (Supplement C), 150-156.
- Du, Y., and C. Lü, (2017). Modeling on monitoring the growth and rupture assessment of saccular aneurysms. *Theoretical and Applied Mechanics Letters* 7(2), 117-120.
- Eskandari, M. K., and S. A. Resnick, (2005). Aneurysms of the Renal Artery. *Seminars in Vascular Surgery* 18(4), 202-208.
- Farotto, D., P. Segers, B. Meuris, J. Vander Sloten, and N. Famaey, (2018). The role of biomechanics in aortic aneurysm management: requirements, open problems and future prospects. *Journal of the Mechanical Behavior of Biomedical Materials*, 77 (Supplement C), 295-307.
- Gates, L., and J. E. Indes, (2017). renal artery aneurysm treatment and management. Retrieved from <https://emedicine.medscape.com/article/463015-treatment>
- Giannoglou, G., G. Giannakoulas, J. Soulis, Y. Chatzizisis, T. Perdikides, N. Melas, N., Parcharidis, G. Louridas, (2006). Predicting the Risk of Rupture of Abdominal Aortic Aneurysms by Utilizing Various Geometrical Parameters: Revisiting the Diameter Criterion. *Angiology* 57(4), 487-494.
- Hoi Yiemeng , Hui Meng, Scott H. Woodward, Bernard R. Bendok, Ricardo A. Hanel, Lee R. Guterman and L. Nelson Hopkins. (2004). Effects of arterial geometry on aneurysm growth: three-dimensional computational fluid dynamics study. *Journal of Neurosurgery* 101(4), 676-681.
- Hwang, P. F., D. C. Rice, S. V. Patel, D. Mukherjee, (2011). Successful management of renal artery aneurysm rupture after cesarean section. *Journal of Vascular Surgery* 54(2), 519-521.
- Javadzadegan, A., B. Fakhim, M. Behnia, and M. Behnia, (2014). Fluid-structure interaction investigation of spiral flow in a model of abdominal aortic aneurysm. *European Journal of Mechanics - B/Fluids* 46 (Supplement C), 109-117.
- Klausner, J. Q., P. F. Lawrence, M. P. Harlander-Locke, D. M. Coleman, J. C. Stanley, and N. Fujimura, (2015). The contemporary management of renal artery aneurysms. *Journal of Vascular Surgery* 61(4), 978-984.e971.
- Kulcsar, Z., L. Augsburg, P. Reymond, V. M. Pereira, S. Hirsch, A. S. Mallik, S. G. Wetzel, I. Wanke, D. A. Rufenacht, (2012). Flow diversion treatment: intra-aneurysmal blood flow velocity and WSS reduction are parameters to predict aneurysm thrombosis. *Acta Neurochir (Wien)* 154(10), 1827-1834.
- Lin, S., X. Han, Y. Bi, S. Ju, and L. Gu, (2017a). Fluid-Structure Interaction in Abdominal Aortic Aneurysm. *BioMed Research International* 2017, 10.
- Lin, S., X. Han, Y. Bi, S. Ju, and L. Gu, (2017b). Fluid-Structure Interaction in Abdominal Aortic Aneurysm: Effect of Modeling Techniques. *BioMed Research International* 2017, 10.
- Maughan, E., C. Webster, T. Konig, and I. Renfrew, (2015). Endovascular management of renal artery aneurysm rupture in pregnancy – A case report. *International Journal of Surgery Case Reports* 12, 41-43.
- Meng, H., Z. Wang, M. Kim, R. D. Ecker, and L. N. Hopkins, (2006). Saccular aneurysms on straight and curved vessels are subject to different hemodynamics: implications of intravascular stenting. *AJNR. American journal of neuroradiology* 27(9), 1861-1865.
- Mokhtar, N. H., A. Abas, N. A. Razak, M. N. A. Hamid, and S. L. Teong, (2017). Effect of different stent configurations using Lattice Boltzmann method and particles image velocimetry on artery bifurcation aneurysm problem. *Journal of Theoretical Biology* 433, 73-84.
- Mokhtar, N. H., A. Abas, S. L. Teong, and N. A. Razak (2016). Particle image velocimetry

- experiment of blood flow through stent in artery bifurcation aneurysm problem. *AIP Conference Proceedings* 1775(1), 030095.
- Mut, F., M. Raschi, E. Scrivano, C. Bleise, J. Chudyk, R. Ceratto, P. Lylyk and J. R. Cebal, (2015). Association between hemodynamic conditions and occlusion times after flow diversion in cerebral aneurysms. *Journal of NeuroInterventional Surgery* 7(4), 286-290.
- Ngoepe, M. N., A. F. Frangi, J. V. Byrne, and Y. Ventikos, (2018). Thrombosis in Cerebral Aneurysms and the Computational Modeling Thereof: A Review. *Frontiers in Physiology* 9(306).
- Orion, K. C., and C. J. Abularrage, (2013). Renal artery aneurysms: movement toward endovascular repair. *Seminars in Vascular Surgery* 26(4), 226-232.
- Otsuka, S., H. Takao, Y. Murayama, S. Masuda, A. Mohamed, Y. Qian, M. Suzuki, M. Yamamoto, and T. Abe (2011). Flow Dynamics in Growing Aneurysms. *Proceedings of the ECCOMAS Thematic International Conference on Simulation and Modeling of Biological Flows (SIMBIO 2011)*.
- Rajah, G., S. Narayanan, and L. Rangel-Castilla, (2017). Update on flow diverters for the endovascular management of cerebral aneurysms. 42(6), E2.
- Raschi, M., F. Mut, G. Byrne, C. M. Putman, S. Tateshima, F. Viñuela, T. Tanoue, K. Tanishita and J. R. Cebal, (2012). CFD and PIV Analysis of Hemodynamics in a Growing Intracranial Aneurysm. *International Journal for Numerical Methods in Biomedical Engineering* 28(2), 214-228.
- Rissland, P., Y. Alemu, S. Einav, J. Ricotta, and D. Bluestein, (2009). Abdominal aortic aneurysm risk of rupture: patient-specific FSI simulations using anisotropic model. *Journal of Biomechanical Engineering* 131(3), 031001.
- Sharzehee, M., S. S. Khalafvand, and H. C. Han, (2018). Fluid-structure interaction modeling of aneurysmal arteries under steady-state and pulsatile blood flow: a stability analysis. *Computer Methods in Biomechanics and Biomedical Engineering* 21(3), 219-231.
- Sisto, A., A. L. Restante, B. A. Brik, and L. Preziosi, (2015, 19-21 Nov. 2015). Numerical simulation comparison between monolayer and Multilayer Flow Modulator in a cerebral saccular aneurysm. *Paper presented at the 2015 E-Health and Bioengineering Conference (EHB)*.
- Soliman, K. B., Y. Shawky, M. M. Abbas, M. Ammary, and A. Shaaban, (2006). Ruptured renal artery aneurysm during pregnancy, a clinical dilemma. *BMC Urology* 6, 22-22.
- Sousa, J., and A. Mansilha, (2017). Endovascular Treatment of Symptomatic Renal Artery Aneurysm with Hostile Anatomy. *Eur J Vasc Endovasc Surg* 53(6), 843.
- Steiger, H. J., R. Aaslid, S. Keller, and H. J. Reulen, (1989). Strength, elasticity and viscoelastic properties of cerebral aneurysms. *Heart and Vessels*, 5(1), 41-46.
- Stergiou, Y. G., A. G. Kanaris, A. A. Mouza, and S. V. Paras, (2019). Fluid-Structure Interaction in Abdominal Aortic Aneurysms: *Effect of Haematocrit Fluids* 4(11).
- Suess, T., J. Anderson, L. Danielson, K. Pohlson, T. Remund, E. Blears, S. Gent and P. Kelly (2016). Examination of near-wall hemodynamic parameters in the renal bridging stent of various stent graft configurations for repairing visceral branched aortic aneurysms. *Journal of Vascular Surgery*, 64(3), 788-796.
- Sultan, S., M. Basuoniy Alawy, R. Flaherty, E. P. Kavanagh, M. Elsherif, A. Elhelali, . . . Hynes, N. (2016). Endovascular management of renal artery aneurysms using the multilayer flow modulator. *Open Heart* 3(1).
- Suzuki, T., H. Takao, S. Fujimura, C. Dahmani, T. Ishibashi, H. Mamori, M. Yamamoto and Y. Murayama, (2017). Selection of helical braided flow diverter stents based on hemodynamic performance and mechanical properties. *Journal of NeuroInterventional Surgery* 9(10), 999-1005.
- Tateshima, S., Y. Murayama, , Villablanca, J., Morino, T., Takahashi, H., Y. Yamauchi, . . . F. Viñuela, (2002). Intraaneurysmal Flow Dynamics Study Featuring an Acrylic Aneurysm Model Manufactured Using a Computerized Tomography Angiogram as a Mold. *Journal of Neurosurgery* 95, 1020-1027.
- Valencia, A., P. Burdiles, M. Ignat, J. Mura, E. Bravo, R. Rivera, and J. Sordo, (2013). Fluid Structural Analysis of Human Cerebral Aneurysm Using Their Own Wall Mechanical Properties. *Computational and Mathematical Methods in Medicine* 2013, 293128.
- Varble, N., G. Trylesinski, J. Xiang, K. Snyder, and H. Meng, (2017). Identification of vortex structures in a cohort of 204 intracranial aneurysms. *Journal of The Royal Society Interface* 14(130).
- Wang, Y., S. Song, G. Zhou, D. Liu, X. Xia, B. Liang, C. Zheng and G. Feng, (2018). Strategy of endovascular treatment for renal artery aneurysms. *Clinical Radiology* 73(4), 414.e411-414.e415.